ARTICLE   OPEN

Exciton-polarons in the presence of strongly correlated electronic states in a MoSe₂/WSe₂ moiré superlattice

Aidan J. Campbell [1], Mauro Brotons-Gisbert [1], Hyeonjun Baek[1], Valerio Vitale[2], Takashi Taniguchi [3], Kenji Watanabe [4], Johannes Lischner[2] and Brian D. Gerardot [1] ✉

Two-dimensional moiré materials provide a highly tunable platform to investigate strongly correlated electronic states. Such emergent many-body phenomena can be optically probed in moiré systems created by stacking two layers of transition metal dichalcogenide semiconductors: optically injected excitons can interact with itinerant carriers occupying narrow moiré bands to form exciton-polarons sensitive to strong correlations. Here, we investigate the behaviour of excitons dressed by a Fermi sea localised by the moiré superlattice of a molybdenum diselenide (MoSe₂)/tungsten diselenide (WSe₂) twisted hetero-bilayer. At a multitude of fractional fillings of the moiré lattice, we observe ordering of both electrons and holes into stable correlated electronic states. Magneto-optical measurements reveal extraordinary Zeeman splittings of the exciton-polarons due to exchange interactions in the correlated hole phases, with a maximum close to the correlated state at one hole per site. The temperature dependence of the Zeeman splitting reveals antiferromagnetic ordering of the correlated holes across a wide range of fractional fillings. Our results illustrate the nature of exciton-polarons in the presence of strongly correlated electronic states and reveal the rich potential of the MoSe₂/WSe₂ platform for investigations of Fermi–Hubbard and Bose–Hubbard physics.

INTRODUCTION

Two-dimensional (2D) materials have emerged as a new play-ground to investigate many-body interactions and strongly correlated electronic phenomena. For example, due to a direct bandgap[1], huge exciton binding energies[2], and straightforward control of carrier concentration[3], monolayer transition metal dichalcogenides (TMDs) provide a platform to probe the interaction of an exciton with a Fermi sea (2D electron or hole gas) described by the Fermi-polaron model[4]. With increasing Fermi energy, a neutral exciton evolves into two branches due to both attractive (lower energy) and repulsive (higher energy) interactions with charge carriers[4–8]. By extension, TMD moiré heterostructures provide access to a highly tunable many-body physical system consisting of an exciton dressed by a Fermi sea which forms a series of charge-ordered (Mott insulating and generalised Wigner crystal) electronic states as the carrier concentration is tuned[9].

Stacking two monolayer TMDs with either a lattice mismatch and/or relative twist angle forms a moiré superlattice with a periodicity that far exceeds the inter-atomic spacing of the constituent crystals. Itinerant electrons in a Fermi sea can be spatially localised by the moiré potential, leading to the formation of flat bands. The suppressed kinetic energy of the charge carriers relative to their on-site Coulomb repulsion energy, U, has led to theoretical predictions[10–16] as well as experimental optical[9,17–22] and transport[23–27] investigations of strongly correlated electron and hole phases for different TMD homo- and hetero-bilayer systems. In the simplest scenario, the highest flat valence band in a TMD moiré system can be mapped onto the 2D triangular Hubbard model[10,12,14]. So far, evidence of Hubbard model physics has only been observed experimentally for angle-aligned WSe₂/WS₂ hetero-bilayers which form a moiré superlattice due to lattice

mismatch[17]. However, the formation and behaviour of exciton-polarons as a function of fractional filling of the moiré lattice in Hubbard model investigations has yet to be probed.

While strongly correlated phenomena have yet to be observed in moiré hetero-bilayers formed from WSe₂ and MoSe₂, the system remains compelling: it is predicted to form flat conduction and valence minibands[28,29] and is an excellent candidate for the realisation of a wide range of strongly correlated states including Wigner crystals[12,13], Mott insulators[10,11,14] and charge-transfer insulators[16]. Compared to TMD hetero-bilayers with different chalcogen atoms, the energetic interplay between Coulomb repulsion and kinetic energy in the WSe₂/MoSe₂ system is more tunable with relative twist angle due to the small (0.2%) lattice mismatch[30]. In addition, the moiré potential in WSe₂/MoSe₂ hetero-bilayers has led to the observation of trapping of interlayer excitons at specific atomic registries in the moiré lattice[31–38]. To date, hetero-bilayer WSe₂/MoSe₂ remains the only moiré system to conclusively exhibit exciton trapping.

Here we optically investigate the formation and behaviour of exciton-polarons, including their charge screening and Coulomb and magnetic interactions, which are formed by intralayer excitons dressed by a Fermi sea localised by a moiré superlattice in a MoSe₂/WSe₂ hetero-bilayer. As the Fermi level is tuned, we observe ordering and re-ordering of itinerant carriers into a multitude of correlated states as evidenced by abrupt changes in the oscillator strength, energy, and linewidth of the exciton-polarons. We observe these correlated states at positive (electron) and negative (hole) fractional fillings (v) of the moiré lattice, including: $v = \pm 1/3, \pm 1/2, \pm 2/3, \pm 1, -5/4$, where $|v| = 1$ represents a single carrier per moiré site. We assign the ± 1 state to be a Mott[17,18,21] or charge-transfer[16] insulator state and the rest to be

[1]Institute of Photonics and Quantum Sciences, SUPA, Heriot-Watt University, Edinburgh EH14 4AS, UK. [2]Departments of Materials and Physics and the Thomas Young Centre for Theory and Simulation of Materials, Imperial College London, South Kensington Campus, London SW7 2AZ, UK. [3]International Center for Materials Nanoarchitectonics, National Institute for Materials Science, 1-1 Namiki, Tsukuba 305-0044, Japan. [4]Research Center for Functional Materials, National Institute for Materials Science, 1-1 Namiki, Tsukuba 305-0044, Japan. ✉email: B.D.Gerardot@hw.ac.uk

generalised Wigner crystals[18,20,21,27]. At $v = -1$ we observe that the repulsive WSe$_2$ exciton-polaron gains oscillator strength from the attractive, due to the reduced screening of the exciton by carriers in the insulating state. After $v = -1$, the oscillator strength is then abruptly transferred to the attractive polaron. Furthermore, we observe filling-factor-dependent g-factors of these positively-charged attractive and repulsive polarons, with a maximum at ~1 hole per site. Under the assumption that the g-factors are proportional to the magnetic susceptibility of the correlated phases induced by exchange interactions, temperature dependent measurements for $v \approx -0.7$ to -1.3 reveal an antiferromagnetic spin coupling of the moiré pinned Fermi-hole sea. The experimental magnetic behaviour is theoretically explored using a model that solves the Heisenberg Hamiltonian for charged-ordered hole states with antiferromagnetic next-neighbour interactions. Our results highlight the behaviour of excitons dressed by a Fermi sea which is spatially ordered in a series of correlated states. This has importance for optical studies of correlated electronic phenomena in 2D materials and demonstrates the potential of MoSe$_2$/WSe$_2$ heterostructures for future investigations and implementations of highly tunable 2D Fermi–Hubbard or Bose–Hubbard models[39].

RESULTS

Device structure and Fermi-polarons

Figure 1a shows a sketch of our dual-gated hetero-bilayer device, consisting of a monolayer MoSe$_2$ and a monolayer WSe$_2$ vertically stacked with a twist angle ($\Delta\theta$) of ~57°. The relative twist angle from perfect H stacking (i.e., $\Delta\theta = 60°$), estimated from the optical micrograph of the hetero-bilayer (see Methods) and confirmed by our gate dependent measurements (described later), is beyond the proposed critical angle for lattice reconstruction[40,41]. The hetero-bilayer was encapsulated by hexagonal boron nitride (hBN) layers with nearly identical thicknesses (~18 nm). Graphene layers act as electrical contacts for the top, bottom and hetero-bilayer gates (see ref. [34] for more details). Moreover, the combination of the layer twist and the lattice mismatch between MoSe$_2$ and WSe$_2$ results in the formation of a triangular moiré superlattice in our device (see sketch in Fig. 1b) with a period of ~6 nm. This causes a periodic variation in the interlayer hopping that results in a flattening of the conduction and valence bands in the type-II band structure characteristic of TMD hetero-bilayers (see Fig. 1c)[42,43]. The bare intralayer excitons of the constituent TMDs can be probed via absorption spectroscopy. The moiré lattice carrier concentration is tuned via the application of a gate voltage (V_g) between the top/bottom graphene contacts and the hetero-bilayer. As depicted by the schematic in Fig. 1b, these carriers are spatially ordered in a series of correlated states by the moiré superlattice, whilst also dressing the photo-excited intralayer exciton to form attractive and repulsive exciton-polaron complexes (as shown in Fig. 1c).

Correlated electronic states

To investigate doping-dependent phenomena, we perform differential reflection contrast ($\Delta R/R_0$) spectroscopy as a function of V_g, where $\Delta R = R_s - R_0$, and R_s (R_0) is the intensity of the light reflected by the hetero-bilayer (substrate). Figure 2a shows the V_g dependence of the first derivative of the reflectance spectra with respect to photon energy (d($\Delta R/R_0$)/dE). The doping dependence of the intralayer exciton-polarons in the MoSe$_2$/WSe$_2$ hetero-bilayer is markedly different to that observed for individual monolayers (see Supplementary Fig. 1). At charge neutrality, we observe three excitonic resonances: X_W^0 at higher energy, and two resonances separated by 36 meV in the spectral range corresponding to X_{Mo}^0, which we label as $X_{Mo,1}^0$ (low energy) and $X_{Mo,2}^0$ (high energy). We assign the two MoSe$_2$ peaks to be a consequence of the formation of moiré minibands, arising from the band folding at the edges of the reduced Brillouin zone[44]. Furthermore, with increasing electron (hole) doping X_W^0 ($X_{Mo,1}^0$) dominate the spectrum, as expected for a type-II band alignment[43,45].

We employ the parallel plate capacitance model to estimate the dependence of the nominal carrier concentration n on the applied V_g. Using the density of moiré sites n_0 corresponding to $\Delta\theta \sim 57°$, we estimate the V_g-dependent nominal fractional filling $v = n/n_0$ of the moiré lattice (see Methods). The excitonic features shown in Fig. 2a exhibit strong modulations in their transition energy, linewidth and oscillator strengths for applied voltages close to the nominal V_g values corresponding to $v = 0$ and ±1. Similar modulations of the excitonic transitions, observed in WSe$_2$/WS$_2$ hetero-bilayers[17,20,21,46], have been attributed to the suppressed charge screening originating from the formation of correlated insulator phases at different fractional fillings of the moiré superlattice. In order to corroborate the presence of a robust moiré lattice at the same spatial position in our sample where we observe strongly correlated states, we measure the low-temperature (4 K) photoluminescence (PL) spectrum at charge neutrality using confocal spectroscopy, revealing a series of
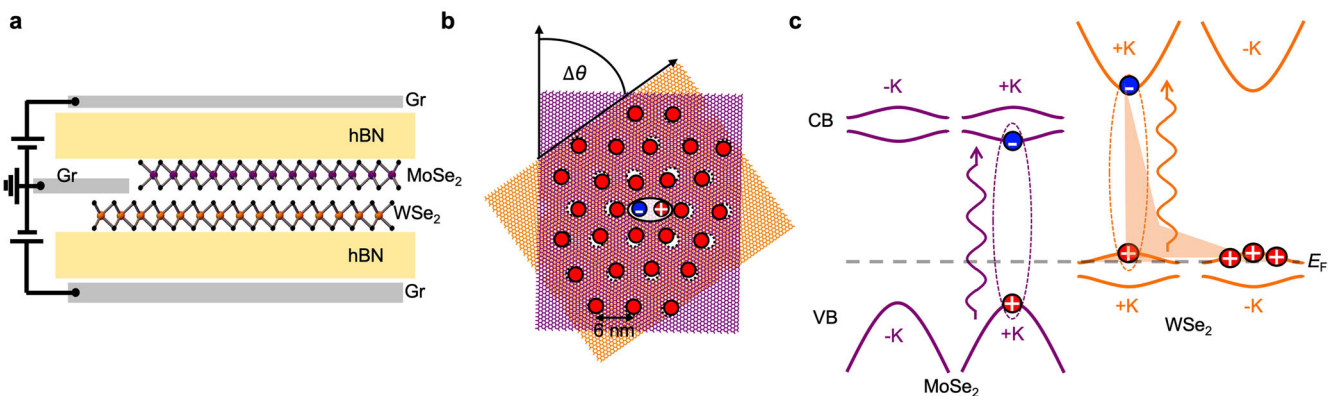

Fig. 1 Device structure. a Sketch of the dual-gated WSe$_2$/MoSe$_2$ hetero-bilayer. Graphene layers are used as top, bottom, and hetero-bilayer electrical contacts, while 18-nm-thick hBN layers are used as dielectric spacers[34]. **b** Illustration of the top view of a moiré superlattice with a twist angle $\Delta\theta$ and fractional filling of one hole per moiré unit cell. Fermi-polarons form between the photo-excited electron-hole pair and charge-ordered Fermi sea. **c** Schematic type-II band structure of the H-WSe$_2$/MoSe$_2$ hetero-bilayer. Purple and orange curves denote bands from MoSe$_2$ and WSe$_2$, respectively. The vertical wavy arrows represent the photon absorption by intralayer excitons in each monolayer. When the Fermi level (E_F) is tuned into the top valence band, the WSe$_2$ attractive polaron forms due to interactions between the exciton in one valley, dressed by holes in the opposite valley.
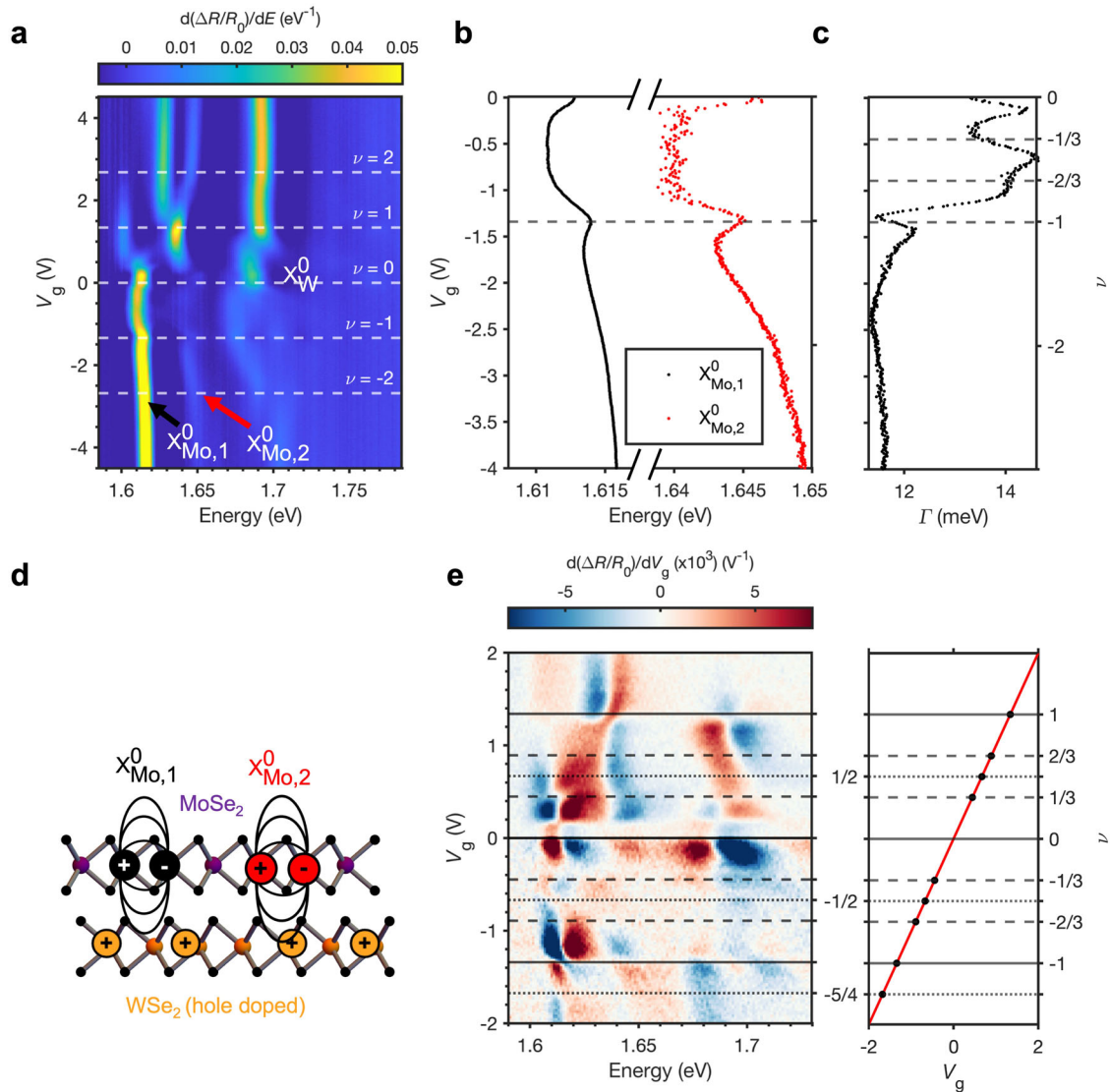
Fig. 2 Correlated electron and hole states in the triangular moiré superlattice of a H-WSe$_2$/MoSe$_2$ hetero-bilayer. a Density plot of the first derivative with respect to energy of the differential reflection contrast ($d(\Delta R/R_0)/dE$) of the MoSe$_2$ and WSe$_2$ intralayer exciton-polarons in the WSe$_2$/MoSe$_2$ hetero-bilayer. **b** Plot of V_g dependence of the estimated peak positions of the MoSe$_2$ excitons. **c** Plot of the V_g dependence of the estimated linewidth Γ of $X^0_{Mo,1}$. **d** Sketch of the concept of dielectric sensing of correlated hole states. **e** Left: density plot of the first derivative with respect to gate voltage of the $\Delta R/R_0$ in panel **a**. $d(\Delta R/R_0)/dV_g$ is multiplied by a factor of 2 for $V_g < 0$ for better visualisation. Right: plot of filling factor v against V_g.

discrete peaks with narrow line-widths (<100 µeV) that demonstrate the existence of an underlying moiré lattice responsible for the interlayer exciton trapping[32–34] (see Supplementary Fig. 2).

Moreover, Fig. 2a also reveals that each monolayer in the WSe$_2$/MoSe$_2$ hetero-bilayer is capable of sensing the doping-induced changes in their dielectric environment originating from the fractional filling of the other layer, similar to the effects observed using a WSe$_2$ sensor layer in proximity to a WSe$_2$/WS$_2$ hetero-structure[21]. Figure 2b shows an example of the sensing capabilities of the MoSe$_2$ layer for hole doping of the WSe$_2$ layer: the transition energies of $X^0_{Mo,1}$ and $X^0_{Mo,2}$ blue-shift and peak at $\Delta V_g = -1.34$ V, consistent with a decrease in the permittivity of the heterostructure arising from the formation of a correlated insulating state at 1 hole per moiré site in the WSe$_2$ layer[17,20]. In addition to the modulation in the transition energy, the linewidth of $X^0_{Mo,1}$ also presents a clear minimum at $v \approx -1$ (see Fig. 2c), which can be understood as the result of reduced charge disorder originating from a correlated insulating state[19]. These results

demonstrate the potential of intralayer excitons as sensors that can probe the formation of correlated states in the adjacent layer (see sketch in Fig. 2d) and corroborate the calibration of $v = \pm 1$ in our device. To estimate the V_g values corresponding to other fractional fillings of the moiré lattice, we assume a linear dependence of v with V_g and extrapolate from the experimental V_g values determined for one hole/electron per site, as shown in the right panel of Fig. 2e. To increase the sensitivity to doping-induced modulations of the reflectance signal, we plot the first derivative of $\Delta R/R_0$ with respect to V_g ($d(\Delta R/R_0)/dV_g$) as a function of V_g (see left panel of Fig. 2e). The $d(\Delta R/R_0)/dV_g$ spectrum highlights a series of abrupt changes in the reflected signal at $v = 0, \pm 1/3, \pm 1/2, \pm 2/3, \pm 1, -5/4$ (as indicated by the horizontal lines in Fig. 2e), suggesting the formation of correlated states at these fractional fillings of the triangular lattice. These results reveal symmetric loading of carriers, with an identical $\Delta V_g = \pm 1.34$ V required to fill the moiré superlattice with either one electron ($V_g = 1.34$ V) or one hole ($V_g = -1.34$ V) per site, respectively. We

assign the stable phases at $v = \pm 1$ to be either Mott[17,18,21] or charge-transfer[16] insulator states and the remaining states to be generalised Wigner crystals[13,18,20,21,27].

To gain deeper insight into the strength of the electronic correlations in our system, we investigate the melting temperature of the different correlated states. Supplementary Fig. 9 shows the dependence of $d(\Delta R/R_0)/dV_g$ on V_g for temperatures ranging from 4 K to 90 K. With increasing temperature, the abrupt changes in the $d(\Delta R/R_0)/dV_g$ spectrum (indicative of correlated state formation in both the electron and hole doping regimes, see Fig. 2e) progressively smooth out until they can no longer be observed at 90 K. We quantitatively estimate a melting temperature of ~55 K for the correlated state at one hole per moiré site (see Supplementary Fig. 10).

Exciton-polaron behaviour at one hole per site

We now investigate the behaviour of the WSe_2 exciton-polarons as the hole fractional filling of the moiré superlattice is tuned. Figure 3a, b shows the σ^-- and σ^+-helicity-resolved evolution of the $d(\Delta R/R_0)/dE$ spectrum, respectively, for negative V_g under an applied magnetic field B of 5 T in Faraday configuration. The intensity colour scale in these figures is saturated to improve the visibility of the WSe_2 intralayer repulsive and attractive exciton-polarons (labelled RP_W^+ and AP_W^+, respectively), while the application of a magnetic field breaks the energy degeneracy between the exciton transitions at $\pm K$, helping to disentangle the behaviour of each excitonic species. As for the monolayer case, at $V_g = 0$ V only the neutral exciton resonance which becomes RP_W^+ is present. As the hole fractional filling increases, an additional resonance gains oscillator strength at ~10 meV lower energy, in agreement with the formation of AP_W^+[47–49].

The helicity-resolved results in Fig. 3a, b reveal additional features of the RP_W^+ and AP_W^+ complexes for fractional hole filling. First, hole doping results in a larger blue-shift of RP_W^+ compared to AP_W^+, as also observed for excitons interacting with a 2D fermionic sea in ML TMDs[4,6,50]. Second, the oscillator strength of the RP_W^+ resonance shows a non-monotonic behaviour: for small gate voltages it decreases with increasing hole doping, which can be understood as a progressive transfer of oscillator strength from the neutral exciton to the positive trion-like state as the Fermi energy moves deeper into the valence band. However, the RP_W^+ resonance regains oscillator strength for hole doping levels corresponding to $v \approx -1$. This can be attributed to the suppressed charge screening in the correlated insulating phase forming in the moiré lattice. For further hole doping ($v < -1$), RP_W^+ abruptly quenches as the oscillator strength transfers to AP_W^+. Third, upon hole doping the σ^+-polarised transitions of both RP_W^+ and AP_W^+ appear at a higher energy than their respective σ^--polarised transitions, indicative of a positive Zeeman splitting ΔE (according to the convention based on $\Delta E = E^{\sigma^+} - E^{\sigma^-}$, with $E^{\sigma^\pm}$ the energy of the transition with $\sigma^\pm$ polarisation). This behaviour contrasts with the negative g-factor of exciton-polarons in ML WSe_2 based on their spin and valley configurations[51].

To gain insight into the origin of the positive Zeeman splitting, we investigate the energies of RP_W^+ and AP_W^+ as a function of the applied B field for $v = -1$. Figure 3c, d shows the σ^-- and σ^+-helicity-resolved evolution of the $d(\Delta R/R_0)/dE$ spectrum for applied B fields
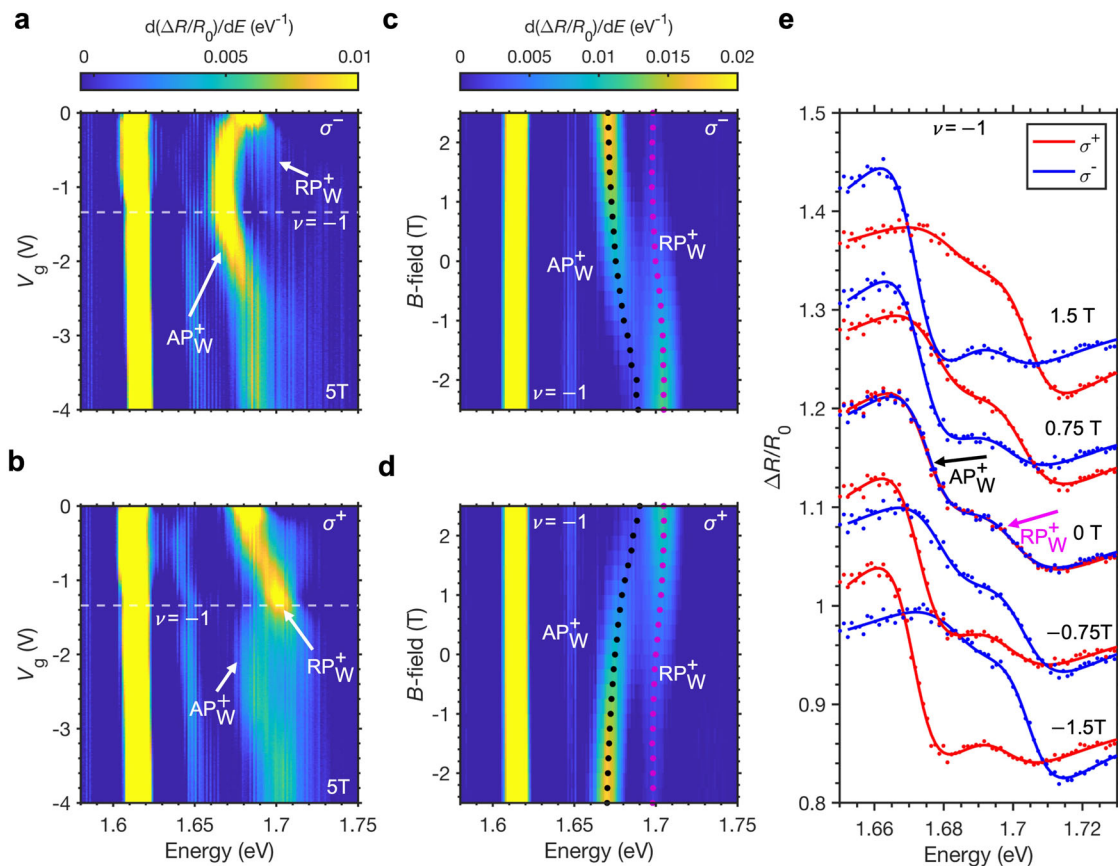

Fig. 3 Exciton-polaron behaviour at one hole per site. a, b σ^-- (**a**) and σ^+-helicity-resolved (**b**) evolution of the first derivative of $\Delta R/R_0$ with respect to energy ($d(\Delta R/R_0)/dE$), as a function of the applied negative V_g (hole doping) under an applied magnetic field of 5 T. **c, d** σ^-- (**c**) and σ^+-helicity-resolved (**d**) evolution of $d(\Delta R/R_0)/dE$ for applied magnetic fields between −2.5 and 2.5 T at $v = -1$. The purple and black dots represent the magnetic-field-dependent estimated energies of the RP_W^+ and AP_W^+, respectively, as extracted from the fits shown in (**e**). **e** Spectra of the bare $\Delta R/R_0$ at different applied magnetic fields (dots) for σ^+- (red) and σ^--polarised (blue) collection. The solid lines represent fits of the experimental $\Delta R/R_0$ to the analytical model described in the Supplementary text.

between −2.5 and 2.5 T at $\nu = -1$. Figure 3e shows linecuts of the bare $\Delta R/R_0$ spectrum at different B fields for σ^+- (red dots) and σ^--polarised (blue dots) collection while the solid lines represent fits from which we estimate the energy, linewidth, and oscillator strength of both RP_W^+ and AP_W^+ as function of the applied magnetic field (see the Supplementary text for a detailed description of the fitting procedure). The B-field-dependent estimated energies of RP_W^+ and AP_W^+ extracted from the fits are overlaid in Fig. 3c, d (purple and black dots, respectively). A large positive Zeeman splitting is clearly observed, which suggests an interaction-enhanced magnetic response of the correlated hole state at $\nu = -1$. Finally, we note that Fig. 3a–e reveal a large spin polarisation of RP_W^+ and AP_W^+ under applied B fields. Such spin polarisation originates from the different effective hole doping in the ±K valleys induced by the large Zeeman splitting. AP_W^+ is an intervalley exciton complex in which the momentum-direct electron-hole pairs at ±K are dressed by holes in the opposite valley[52,53]. On application of a positive magnetic field

of 5 T, the valence band edge at +K is shifted to higher energy relative to −K. Exchange interactions favour single valley occupancy of carriers, so nearly all the holes are doped in the +K valley, rather than the −K, leading to the observed spin polarisation[6]. When we probe the exciton in −K using σ^- light, there is a large population of holes available to form AP_W^+ (see Fig. 3a). In contrast, there is a smaller population of holes at −K available to form AP_W^+ when we probe the +K exciton using σ^+, leading to a higher relative intensity of RP_W^+ (see Fig. 3b). When we sweep the magnetic field from positive to negative, we shift the band maximum from +K to −K, leading to the observed transfer in oscillator strength between RP_W^+ and AP_W^+ (see Fig. 3c–e).

Magnetic interactions probed by exciton-polarons

Next, we investigate the fractional-filling-dependence of the Zeeman splitting of the RP_W^+ and AP_W^+ resonances. Figure 4a
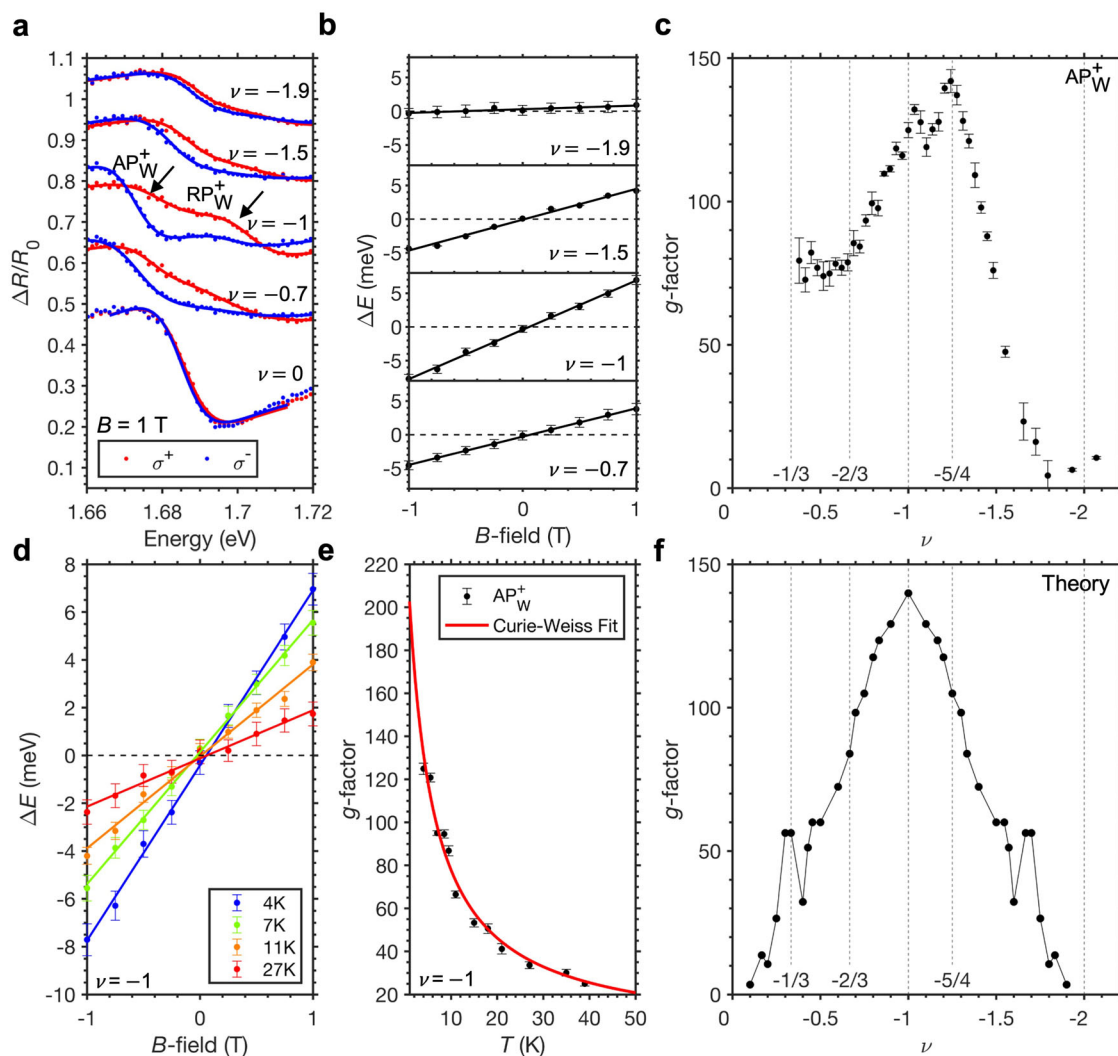

Fig. 4 Exciton-polaron magnetic interactions at different hole fractional fillings. a σ^-- (blue) and σ^+-resolved (red) $\Delta R/R_0$ spectra at representative hole ν values under a $B = 1$ T. **b** B-field-dependent Zeeman splitting of AP_W^+ from −1 to 1 T at representative hole ν values. **c** Evolution of the g-factor of AP_W^+ as a function of the hole ν extracted from linear fits of ΔE in the range $|B| \leq 1$ T (solid lines in panel **b**). **d** Valley Zeeman splitting of the AP_W^+ resonance at $\nu = -1$ for different temperatures. **e** Evolution of the measured g-factor of AP_W^+ as a function of temperature for $\nu = -1$ in the temperature range for which the oscillator strength and linewidth of AP_W^+ are sufficient to enable a reliable estimate of the Zeeman splitting. The red solid line represents a fit of the experimental data (black dots) to a Curie–Weiss law from which the Weiss constant is estimated to be $\theta = -4.6 \pm 0.9$ K. The negative sign of the extracted Weiss constant reveals antiferromagnetic ordering of neighbouring hole spins. **f** Theoretical prediction of the ν dependence of the g-factor based on a model that solves the Heisenberg Hamiltonian for charge-ordered hole states with antiferromagnetic exchange interactions between nearest neighbour spins. For all panels the error bars represent 68% confidence intervals.

shows σ^-- (blue) and σ^+-resolved (red) $\Delta R/R_0$ spectra at representative hole v values at $B = 1$ T. The dots represent experimental data while the solid lines are fits of the experimental $\Delta R/R_0$ to the model described in the Supplementary text, from which we estimate the energy of the resonances. The spectra in Fig. 4a reveal a clear positive ΔE for all hole doping levels, although with a magnitude that depends strongly on v. Figure 4b shows the B-field-dependent Zeeman splitting of AP_W^+ from -1 to 1 T at representative hole v values. The estimated Zeeman splitting exhibits a linear dependence with B at small fields (i.e., $|B| < 1$ T). We note that RP_W^+ shows a similar positive linear dependence with B at small fields, although it saturates at larger B (see Supplementary Fig. 6). The linear evolution of ΔE at small B can be associated to an effective exciton valley g-factor according to $\Delta E(B) = g\mu_0 B$, where μ_0 is the Bohr magneton. Figure 4c shows the evolution of the g-factor of AP_W^+ as a function of the hole v extracted from linear fits of ΔE in the range $|B| \leq 1$ T (solid lines in Fig. 4b). As already inferred from the results in Fig. 4b, the g-factor of AP_W^+ shown in Fig. 4c exhibits a strong dependence on v, peaking around $v \approx -1$, where it reaches a maximum value of $g \sim 145$.

Figure 4d shows the Zeeman splitting of AP_W^+ measured for $|B| \leq 1$ T at $v = -1$ for different temperatures, where we observe the slope of the Zeeman splitting (and therefore the g-factor) decreases with increasing temperature. Figure 4e shows the evolution of the measured g-factor of AP_W^+ as a function of temperature for $v = -1$ in the temperature range in which the oscillator strength and linewidth of AP_W^+ enable a reliable estimate. We observe that the g-factor decreases by a factor ~5 when the temperature increases from 4 to 39 K. We assume that the interaction-induced enhancement of the attractive polaron g-factor is proportional to the magnetic susceptibility of the correlated states (e.g., $\chi \propto g$) and observe that the decrease of g-factor with increasing temperature follows a Curie–Weiss law $\chi^{-1} \propto T - \theta$ (red solid line in Fig. 4e), with T being the temperature and θ the Weiss constant. From the fit in Fig. 4e we estimate a Weiss constant of $\theta = -4.6 \pm 0.9$ K, which suggests an antiferromagnetic behaviour of the interactions between the localised hole moments for $v = -1$. Supplementary Fig. 11 shows the temperature dependence of the AP_W^+ g-factor for a range of hole filling factors from $v = -0.7$ to $v = -1.37$. The Weiss constants extracted from the Curie–Weiss fits are negative for all the explored hole filling factors, suggesting an antiferromagnetic phase for all correlated hole states. We note we observe no magnetic hysteresis in the Zeeman splitting at $v = -1$ when the magnetic field is swept from negative to positive values followed by a subsequent positive to negative sweep (see Supplementary Fig. 7). In contrast to the large attractive polaron g-factor enhancement observed under hole doping, we only observe a modest g-factor enhancement in the electron doping regime (see Supplementary Fig. 8).

DISCUSSION

The extraordinary g-factors observed under hole doping can be understood by considering the effect of a magnetic field on a localised hole in the triangular moiré superlattice. As a result of exchange interactions with other holes in its environment, such a hole experiences an effective magnetic field which is the sum of the externally applied field and the field induced by the other holes which in turn is proportional to the magnetisation M of the localised hole gas (i.e., $\propto \lambda_X M$, with λ_X being a coupling constant).

To calculate the induced field for a given fractional filling, we first determine the configuration of localised carriers that minimises the electrostatic repulsion energy using a simulated annealing technique (see Supplementary text for details). To describe the spin response of this arrangement of charges, we consider a Heisenberg Hamiltonian with distance-dependent antiferromagnetic isotropic exchange interactions $J(r) = J_0 \exp(-r/r_0)$ with J_0 denoting the

magnitude of the exchange coupling at the characteristic length scale r_0. For this Hamiltonian, the induced magnetic field and the corresponding g-factor enhancement, g^*/g, of a localised hole are calculated within mean-field theory (see Supplementary text for a detailed description). To obtain the effective g-factor of the attractive exciton-polaron which is probed in our experiments, we assume that its g-factor enhancement due to exchange interactions with localised holes is the same as that of a single hole, but that the 'non-enhanced' g-factor g can be different. The experimental value of this non-enhanced g is unknown since the g-factors of exciton-polarons are dependent on paramagnetic interactions and phase-space filling effects as carrier concentration is changed, even for monolayer TMDs[6]. Therefore, we treat g as an adjustable parameter choosing its value such that the calculated and experimentally measured g-factors agree at $v = -1$.

Figure 4f shows that the filling dependence of the calculated g-factor is in good qualitative agreement with the experimental results. Specifically, it reaches a maximum at $v = -1$, where the average number of occupied moiré sites around the localised hole is largest and the strong exchange interactions between neighbouring spins give rise to a large effective magnetic field. The model also captures the plateau-like feature between $v = -1/3$ and $-2/3$. In contrast to the experimental findings, however, the calculated g-factor is symmetric around $v = -1$. Potential reasons for this discrepancy include (i) band structure effects and (ii) the doping-induced reduction of frustration. Regarding (i), Tang et al. pointed out that the maximum g-factor occurs at a filling factor that corresponds to a van Hove singularity of the density of states[17]. Regarding (ii), Zhang et al. carried out exact diagonalisation studies of a triangular t-J model and found that at finite temperatures the maximum spin susceptibility occurs at a hole filling higher than $v = -1$[16]. This is in agreement with a study by Koretsune et al. which employs a high-temperature expansion of the spin response function[54]. The increase in the spin susceptibility was explained in the work by the "release" of frustration by doping. Further theoretical work is required to fully understand the detailed behaviour of the g-factor.

Finally, we estimate U/t in our device. The antiferromagnetic coupling between neighbouring spins due to the kinetic exchange mechanism can be estimated as $J \approx -t^2/U$, where t is the hopping amplitude between neighbouring moiré lattice sites. Using the value of θ at $v = -1$ we estimate $J \approx -0.4$ meV. By combining J with the estimated melting temperature of the correlated state at $v = -1$ (~55 K) we obtain $U/t \approx 3.5 \pm 0.4$. This experimental value agrees well with predicted values for MoSe$_2$/WSe$_2$ heterostructures with stacking angles ~3° and ~57°[10].

Our results illustrate the properties of exciton-polarons in the presence of correlated states in moiré heterostructures. Using the changes in energy, oscillator strength, and linewidth of intralayer excitons dressed by itinerant carriers occupying narrow electronic moiré bands in a MoSe$_2$/WSe$_2$ hetero-bilayer, we observe the formation of correlated electron and hole states at a multitude of fractional fillings of the moiré lattice. Upon hole doping, the WSe$_2$ attractive polaron transfers oscillator strength back to the repulsive polaron branch at 1 carrier per site, demonstrating the reduced screening of the exciton by the free charges in the presence of the insulating state. In addition, we observe the magnetic interactions within the correlated hole states via both the attractive and repulsive WSe$_2$ exciton-polarons, which exhibit enhanced Zeeman splittings due to exchange interactions with the moiré pinned carriers. Through temperature dependent measurements, the magnetic ordering of the correlated holes is shown to be antiferromagnetic in the range $v = -0.7$ to $v = -1.37$, and the U/t ratio of our device is estimated to be ~3.5. Further investigations could exploit the small lattice mismatch between MoSe$_2$/WSe$_2$, which enables a highly tunable moiré period, to simulate condensed matter phase diagrams over a large range of U/t ratios. Our observation of the formation of flat electronic

METHODS

Sample fabrication

The sample was fabricated using the all-dry viscoelastic transfer technique[55]. Bulk crystal was exfoliated onto PDMS stamps and monolayer flakes were identified using an optical microscope. As shown in a previous work for the same sample studied in this work, the zigzag edges of the TMD monolayers were identified using optical images in order to achieve a nearly angle-aligned heterostructure (0° or 60°). Further details can be found in[34]. The interface between the two TMD layers is kept pristine (free of polymer contamination) by a transfer of one flake from its PDMS stamp onto the other flake on its PDMS stamp before subsequent transfer onto the bottom hBN layer of the device. The twist angle is estimated to be ~57° from the optical images. Gold contacts to the graphene layers were fabricated using standard lithography techniques.

Optical measurements

The sample is held in a closed-cycle cryostat at 4 K unless otherwise specified (for temperature dependent measurements). For differential reflectivity measurements, light from a power stabilised tungsten lamp is collected by a multi-mode fibre. The light is collimated by a 20× objective and focused on the sample with an achromatic objective (0.82 numerical aperture). The reflected light is collected with the same objective and then focused onto a single-mode fibre and detected using a liquid nitrogen-cooled CCD spectrometer. The setup is confocal in collection due to the small diameter of the core of the collection fibre. The incident and collected polarisation of the light is controlled using a series of linear polarisers, quarter-wave and half-wave plates.

Filling factor calibration

The carrier concentration n in the heterostructure can be calculated using the parallel plate capacitance model, $n = \frac{\epsilon\epsilon_0 \Delta V_g}{d_1} + \frac{\epsilon\epsilon_0 \Delta V_g}{d_2}$ where ϵ is the permittivity of hBN, ΔV_g is the voltage offset between both the top and bottom gates and the heterostructure gate, and d_1 (d_2) is the thickness of the top (bottom) hBN layer measured to be 17.4 ± 0.2 nm (18.2 ± 0.3 nm) using nulling ellipsometry. For a small angular difference between two stacked layers the moiré periodicity can be estimated using $\lambda_M = \frac{a_{Se}}{\sqrt{\delta^2 + \theta^2}}$ where a_{Se} is the lattice constant of WSe$_2$, δ is the fractional lattice mismatch between the two layers and θ is the twist angle in radians. For a triangular moiré pattern, the number of carriers required for one hole per site is given by $n_0 = \frac{2}{\sqrt{3}\lambda_M^2}$. Using the lattice constants of 0.3280 and 0.3288 nm for WSe$_2$ and MoSe$_2$, respectively[30] and a permittivity of 3.8 for the hBN[56], and $\Delta V_g = 1.34$ V for $\nu = \pm 1$ as determined in the main text, we calculate the twist angle in the main measurement location to be 56.9°. This agrees well with the angle of ~57° estimated from the optical micrograph.

DATA AVAILABILITY

Data described in this paper are available online at https://researchportal.hw.ac.uk/en/persons/brian-d-gerardot/datasets/.

CODE AVAILABILITY

All relevant codes are available from the corresponding author on request.

REFERENCES

1. Splendiani, A. et al. Emerging photoluminescence in monolayer MoS$_2$. *Nano Lett.* **10**, 1271–1275 (2010).
2. Chernikov, A. et al. Exciton binding energy and nonhydrogenic Rydberg series in monolayer WS$_2$. *Phys. Rev. Lett.* **113**, 076802 (2014).
3. Baugher, B. W. H., Churchill, H. O. H., Yang, Y. & Jarillo-Herrero, P. Optoelectronic devices based on electrically tunable p–n diodes in a monolayer dichalcogenide. *Nat. Nanotechnol.* **9**, 262–267 (2014).
4. Sidler, M. et al. Fermi polaron-polaritons in charge-tunable atomically thin semiconductors. *Nat. Phys.* **13**, 255–261 (2017).
5. Suris, R. A. et al. Excitons and trions modified by interaction with a two-dimensional electron gas. *Phys. Status Solidi B* **227**, 343–352 (2001).
6. Back, P. et al. Giant paramagnetism-induced valley polarization of electrons in charge-tunable monolayer MoSe$_2$. *Phys. Rev. Lett.* **118**, 237404 (2017).
7. Efimkin, D. K. & MacDonald, A. H. Many-body theory of trion absorption features in two-dimensional semiconductors. *Phys. Rev. B* **95**, 035417 (2017).
8. Glazov, M. M. Optical properties of charged excitons in two-dimensional semiconductors. *J. Chem. Phys.* **153**, 034703 (2020).
9. Shimazaki, Y. et al. Strongly correlated electrons and hybrid excitons in a moiré heterostructure. *Nature* **580**, 472–477 (2020).
10. Wu, F., Lovorn, T., Tutuc, E. & MacDonald, A. H. Hubbard model physics in transition metal dichalcogenide moiré bands. *Phys. Rev. Lett.* **121**, 026402 (2018).
11. Naik, M. H. & Jain, M. Ultraflatbands and shear solitons in moiré patterns of twisted bilayer transition metal dichalcogenides. *Phys. Rev. Lett.* **121**, 266401 (2018).
12. Pan, H., Wu, F. & Sarma, S. D. Quantum phase diagram of a Moiré-Hubbard model. *Phys. Rev. B* **102**, 201104 (2020).
13. Padhi, B., Chitra, R. & Phillips, P. W. Generalized Wigner crystallization in moiré materials. *Phys. Rev. B* **103**, 125146 (2021).
14. Morales-Durán, N., MacDonald, A. H. & Potasz, P. Metal-insulator transition in transition metal dichalcogenide heterobilayer moiré superlattices. *Phys. Rev. B* **103**, L241110 (2021).
15. Zang, J., Wang, J., Cano, J. & Millis, A. J. Hartree-Fock Study of the Moiré Hubbard model for twisted bilayer transition metal dichalcogenides. *Phys. Rev. B* **104**, 075150 (2021).
16. Zhang, Y., Yuan, N. F. & Fu, L. Moiré quantum chemistry: charge transfer in transition metal dichalcogenide superlattices. *Phys. Rev. B* **102**, 201115 (2020).
17. Tang, Y. et al. Simulation of Hubbard model physics in WSe$_2$/WS$_2$ moiré superlattices. *Nature* **579**, 353–358 (2020).
18. Regan, E. C. et al. Mott and generalized Wigner crystal states in WSe$_2$/WS$_2$ moiré superlattices. *Nature* **579**, 359–363 (2020).
19. Zhou, Y. et al. Bilayer Wigner crystals in a transition metal dichalcogenide heterostructure. *Nature* **595**, 48–52 (2021).
20. Liu, E. et al. Excitonic and valley-polarization signatures of fractional correlated electronic phases in a WSe$_2$/WS$_2$ Moiré Superlattice. *Phys. Rev. Lett.* **127**, 037402 (2021).
21. Xu, Y. et al. Correlated insulating states at fractional fillings of moiré superlattices. *Nature* **587**, 214–218 (2020).
22. Miao, S. et al. Strong interaction between interlayer excitons and correlated electrons in WSe$_2$/WS$_2$ moiré superlattice. *Nat. Commun.* **12**, 3608 (2021).
23. Wang, L. et al. Correlated electronic phases in twisted bilayer transition metal dichalcogenides. *Nat. Mater.* **19**, 861–866 (2020).
24. Li, T. et al. Continuous Mott transition in semiconductor moiré superlattices. *Nature* **597**, 350–354 (2021).
25. Ghiotto, A. et al. Quantum criticality in twisted transition metal dichalcogenides. *Nature* **597**, 345–349 (2021).
26. Li, T. et al. Charge-order-enhanced capacitance in semiconductor moiré superlattices. *Nat. Nanotechnol.* **16**, 1068–1072 (2021).
27. Huang, X. et al. Correlated insulating states at fractional fillings of the WS$_2$/WSe$_2$ moiré lattice. *Nat. Phys.* **17**, 715–719 (2021).
28. Ruiz-Tijerina, D. A. & Fal'ko, V. I. Interlayer hybridization and moiré superlattice minibands for electrons and excitons in heterobilayers of transition-metal dichalcogenides. *Phys. Rev. B* **99**, 125424 (2019).
29. Vitale, V., Atalar, K., Mostofi, A. A. & Lischner, J. Flat band properties of twisted transition metal dichalcogenide homo-and heterobilayers of MoS$_2$, MoSe$_2$, WS$_2$ and WSe$_2$. *2D Mater.* **8**, 045010 (2021).

30. Brixner, L. H. Preparation and properties of the single crystalline ab2-type selenides and tellurides of niobium, tantalum, molybdenum and tungsten. *J. Inorg. Nucl. Chem* **24**, 257–263 (1962).

31. Yu, H., Liu, G.-B., Tang, J., Xu, X. & Yao, W. Moiré excitons: from programmable quantum emitter arrays to spin-orbit–coupled artificial lattices. *Sci. Adv.* **3**, e1701696 (2017).

32. Seyler, K. L. et al. Signatures of moiré-trapped valley excitons in $MoSe_2/WSe_2$ heterobilayers. *Nature* **567**, 66–70 (2019).

33. Brotons-Gisbert, M. et al. Spin-layer locking of interlayer excitons trapped in moiré potentials. *Nat. Mater.* **19**, 630–636 (2020).

34. Baek, H. et al. Highly energy-tunable quantum light from moiré-trapped excitons. *Sci. Adv.* **6**, eaba8526 (2020).

35. Liu, E. et al. Signatures of moiré trions in $WSe_2/MoSe_2$ heterobilayers. *Nature* **594**, 46–50 (2021).

36. Brotons-Gisbert, M. et al. Moiré-trapped interlayer trions in a charge-tunable $WSe_2/MoSe_2$ heterobilayer. *Phys. Rev. X* **11**, 031033 (2021).

37. Baek, H. et al. Optical read-out of Coulomb staircases in a moiré superlattice via trapped interlayer trions. *Nat. Nanotechnol.* **16**, 1237–1243 (2021).

38. Wang, X. et al. Moiré trions in $MoSe_2/WSe_2$ heterobilayers. *Nat. Nanotechnol.* **16**, 1208–1213 (2021).

39. Kennes, D. M. et al. Moiré heterostructures as a condensed-matter quantum simulator. *Nat. Phys.* **17**, 155–163 (2021).

40. Rosenberger, M. R. et al. Twist angle-dependent atomic reconstruction and moiré patterns in transition metal dichalcogenide heterostructures. *ACS Nano* **14**, 4550–4558 (2020).

41. Weston, A. et al. Atomic reconstruction in twisted bilayers of transition metal dichalcogenides. *Nat. Nanotechnol.* **15**, 592–597 (2020).

42. Chiu, M.-H. et al. Determination of band alignment in the single-layer MoS_2/WSe_2 heterojunction. *Nat. Commun.* **6**, 7666 (2015).

43. Wilson, N. R. et al. Determination of band offsets, hybridization, and exciton binding in 2D semiconductor heterostructures. *Sci. Adv.* **3**, e1601832 (2017).

44. Wu, F., Lovorn, T. & MacDonald, A. H. Topological exciton bands in moiré heterojunctions. *Phys. Rev. Lett.* **118**, 147401 (2017).

45. Hong, X. et al. Ultrafast charge transfer in atomically thin MoS_2/WS_2 heterostructures. *Nat. Nanotechnol.* **9**, 682–686 (2014).

46. Jin, C. et al. Stripe phases in WSe_2/WS_2 moiré superlattices. *Nat. Mater.* **20**, 940–944 (2021).

47. Wang, Z., Zhao, L., Mak, K. F. & Shan, J. Probing the spin-polarized electronic band structure in monolayer transition metal dichalcogenides by optical spectroscopy. *Nano Lett.* **17**, 740–746 (2017).

48. Van Tuan, D. et al. Probing many-body interactions in monolayer transition-metal dichalcogenides. *Phys. Rev. B* **99**, 085301 (2019).

49. Courtade, E. et al. Charged excitons in monolayer WSe_2: Experiment and theory. *Phys. Rev. B* **96**, 085302 (2017).

50. Roch, J. G. et al. Spin-polarized electrons in monolayer MoS_2. *Nat. Nanotechnol.* **14**, 432–436 (2019).

51. Förste, J. et al. Exciton g-factors in monolayer and bilayer WSe_2 from experiment and theory. *Nat. Commun.* **11**, 4539 (2020).

52. Wang, T. et al. Observation of quantized exciton energies in monolayer WSe_2 under a strong magnetic field. *Phys. Rev. X* **10**, 021024 (2020).

53. Liu, E. et al. Landau-quantized excitonic absorption and luminescence in a monolayer valley semiconductor. *Phys. Rev. Lett.* **124**, 097401 (2020).

54. Koretsune, T. & Ogata, M. Resonating-valence-bond states and ferromagnetic correlations in the doped triangular Mott insulator. *Phys. Rev. Lett.* **89**, 116401 (2002).

55. Castellanos-Gomez, A. et al. Deterministic transfer of two-dimensional materials by all-dry viscoelastic stamping. *2D Mater.* **1**, 011002 (2014).

56. Laturia, A., Van de Put, M. L. & Vandenberghe, W. G. Dielectric properties of hexagonal boron nitride and transition metal dichalcogenides: from monolayer to bulk. *npj 2D Mater. Appl.* **2**, 6 (2018).

AUTHOR CONTRIBUTIONS

B.D.G. conceived and supervised the project. H.B. fabricated the sample. K.W. and T.T. supplied the hBN crystal. A.J.C. performed the experiment assisted by M.B.-G. A.J.C. analysed the data, assisted by M.B.-G. and B.D.G. V.V. and J.L. developed the theoretical model. A.J.C., M.B.-G., V.V., J.L. and B.D.G. cowrote the paper with input from all authors.

COMPETING INTERESTS

The authors declare no competing interests.

ADDITIONAL INFORMATION

Supplementary information The online version contains supplementary material available at https://doi.org/10.1038/s41699-022-00358-w.

Correspondence and requests for materials should be addressed to Brian D. Gerardot.

Reprints and permission information is available at http://www.nature.com/reprints

Publisher's note Springer Nature remains neutral with regard to jurisdictional claims in published maps and institutional affiliations.